We are IntechOpen, the world's leading publisher of Open Access books
Built by scientists, for scientists

4,800
Open access books available

122,000
International authors and editors

135M
Downloads

154
Countries delivered to

Our authors are among the
TOP 1%
most cited scientists

12.2%
Contributors from top 500 universities

WEB OF SCIENCE™

Selection of our books indexed in the Book Citation Index in Web of Science™ Core Collection (BKCI)

Interested in publishing with us?
Contact book.department@intechopen.com

Numbers displayed above are based on latest data collected.
For more information visit www.intechopen.com

Chapter

Silicon Nanocrystals and Amorphous Nanoclusters in SiO_x and SiN_x: Atomic, Electronic Structure, and Memristor Effects

Vladimir Volodin, Vladimir Gritsenko, Andrei Gismatulin and Albert Chin

IntechOpen

Abstract

Semiconductor nanocrystals in dielectric films are interesting from fundamental aspect, because quantum-size effects in them appear even at room temperature, so such objects can be called as "quantum dots". Silicon nanocrystals and amorphous silicon nanoclusters in substoichiometric SiO_x and SiN_x films are traps for electrons and holes that apply in nonvolatile memory devices. In this chapter the formation of silicon nanocrystals and silicon amorphous nanoclusters in SiO_x and SiN_x films was studied using structural and optical methods. The phonon confinement model was refined to obtain sizes of silicon nanocrystals from analysis of Raman scattering data. Structural models that lead to nanoscale potential fluctuation in amorphous SiO_x and SiN_x are considered. A new structural model which is intermediate between random mixture and random bonding models is proposed. Memristor effects in SiO_x films are discussed.

Keywords: silicon suboxides, silicon subnitrides, nanocrystals, amorphous nanoclusters, phonon confinement model, nanoscale potential fluctuations, memristor

IntechOpen

1. Introduction

Nanometer-sized semiconductor crystals, the so-called nanocrystals (NCs) and amorphous nanoclusters, embedded in wide-gap insulating matrices, have shown significant promises for application in nanoelectronics (nonvolatile memory) and optoelectronics (light-emitting diodes (LEDs)) [1]. Quantum effects in such hetero-systems are manifested even at room temperature. For example, a bright photoluminescence (PL) was observed in dodecyl-passivated colloidal Si NCs with external quantum efficiency (QE) up to 60% [2]. Since in some experiments single NCs originated delta-function-like energy photoluminescence spectra [3], they can be called as quantum dots. In metal-dielectric-semiconductor structures based on SiN_x films with Si nanoclusters, an effective electroluminescence with red, green, and blue light-emitting diodes was demonstrated [4]. Since NCs in a dielectric matrices act also as traps for charge carriers, the NCs' based structures have also

perspectives to yield nonvolatile memory devices [5]. Last time the perspectives of application of nonstoichiometric SiO_x and SiN_x films with Si NCs and amorphous nanoclusters in memristors have arisen [6]. This chapter is devoted to formation, structural and optical studies of such films, and the development of new structural models which would explain the presence of nanoscale potential fluctuations in such nonstoichiometric films.

2. Forming of Si NCs and amorphous nanoclusters in dielectric films

There are several technological approaches for the fabrication of Si NCs and amorphous Si nanoclusters in various dielectric films: Si^+ ion implantation with consequent thermal annealing; co-sputtering of Si and SiO_2 targets on cool substrates; chemical vapor deposition (CVD) and plasma-enhanced chemical vapor deposition (PECVD) methods; evaporation of Si, SiO, or SiO_2 under high vacuum and their deposition onto cool substrates; evaporation of Si target in atmosphere with definite partial pressure of oxygen; and deposition on cool substrates. Each method has advantages and peculiarities.

The main advantage of ion implantation is a very precise control of the dose of the embedded silicon atoms—control of the projected range of silicon ions (it depends on the energy of ions). The disadvantage is the need for high-temperature annealing for the formation of silicon nanoclusters and even more high-temperature annealing (up to 1150°C) for their crystallization. So, this process cannot be “back-end-of-line” process in device production.

The benefits of different approaches that use co-sputtering are simplicity, the possibility to control stoichiometry using various intensity of evaporation of the targets, and the opportunity to use different substrates. The CVD and PECVD methods allow using large-scale substrates; the control of stoichiometry is possible using different ratios of reagent gases. The main advantage of PECVD is low temperature of the deposition process, but because almost all reagent gases contain hydrogen, the deposited SiO_x and SiN_x films are hydrogenated; in this case they should be marked as SiO_x:H and SiN_x:H films. Sometimes the hydrogen content is undesirable because it leads to instability of the characteristics of the films.

It should be noted that applying of various deposition methods leads to variation of the structural model of nonstoichiometric films. The structure of nonstoichiometric SiO_x or SiN_x films can be described in the framework of the random mixture (RM) or random bonding (RB) models [7]. In the RM model, SiO_x is treated as a mixture of two phases: the stoichiometric phase SiO_2 and the Si. In the RB model, SiO_x is assumed to consist of Si—O(ν)/Si($4-\nu$) structural units, ν = 0, 1, 2, 3, or 4, in which Si atoms statistically substitute O atoms in each Si—O(4) structural unit. The structure of films formed by ion implantation and co-sputtering with ion beam evaporation of targets is closer to RB model; the structure of PECVD films can be closer to RM model. But structure of real films is always not pure RB or pure RM, and real structure of the films (which is the cause of nanoscale potential fluctuations in nonstoichiometric films) will be discussed below.

3. Raman scattering in SiO_x and SiN_x films: phonon confinement in Si NCs

Direct methods for studying the structure of nonstoichiometric films (such as high-resolution transmission electron microscopy (HRTEM)) are usually very time-consuming and destructive. Optical methods for studying the structure of NCs

and amorphous nanoclusters are nondestructive and express. Among the optical methods, the most informative is inelastic light scattering—Raman scattering.

Raman scattering measurements are usually carry out to check the presence of a crystalline or amorphous Si phase in as-deposited and annealed SiO_x and SiN_x films. Due to the absence of long-range order and breaking of translation symmetry, the Raman spectrum of amorphous Si is an image of effective density of vibrational states for transversal optical (TO) and transversal acoustical (TA) modes and contains two broad peaks at approximately 480 and 150 cm^{-1}, correspondingly [8]. According to the quasi-momentum selection rules, in monocrystalline silicon, only phonons from the center of the Brillouin zone are active in Raman scattering; therefore the frequency of the Raman peak in this case is 520.5 cm^{-1} [9], and the full width on half maximum (FWHM) usually is about 5 cm^{-1}; it is much narrower than the width of amorphous peak. The intensity of the crystalline peak depends on the contents of the crystalline phase, and, using the analysis of experimentally measured integrated Raman scattering intensities I_c and I_a for c-Si and a-Si phases, one can obtain the volume part of crystalline phase in a two-phase film. The critical parameter of this method is the ratio of the integrated Raman cross section for c-Si to a-Si, $y = \Sigma_c/\Sigma_a$. Knowing this parameter, one can use the next equation:

$$\rho_c = I_c/(I_c + yI_a) \tag{1}$$

Recently, we have clarified the Bustarret data [10] on the dependence of the parameter y on the size of nano- and micro silicon crystals [11].

Due to softening of the conservation law of quasi-momentum in NCs, the short-wave phonons can take part in Raman scattering in this case. The confined in NCs phonons are characterized by a narrow peak at a position of 500–520 cm^{-1}. The position and the width of the peak strongly depend on the size and structure of the NCs [12, 13]. We have developed an improved phonon confinement model (PCM) for the analysis of average size of Si NCs from Raman data.

PCM allows us to calculate the Raman spectra for NCs of various sizes [12–14]. The physical entity of the model is the following. The eigenfunction of phonon with quasi-momentum $\hbar\mathbf{q_0}$ in an infinite crystal is

$$\Phi(\mathbf{q_0}, \mathbf{r}) = u(\mathbf{r})\ e^{i\,\mathbf{q_0}\,\mathbf{r}}, \tag{2}$$

where $u(\mathbf{r})$ has the periodicity of the lattice and $\mathbf{q_0}$ is the wavenumber of phonon.

The eigenfunction $\Psi(\mathbf{q_0}, \mathbf{r})$ for a phonon confined in NCs is a function $\Phi(\mathbf{q_0}, \mathbf{r})$ multiplied by the phonon weighting function $W(\mathbf{r},\ L)$ ("envelope" function for displacement of atoms in NCs); the weighting function depends on NC size L:

$$\Psi(\mathbf{q_0}, \mathbf{r}) = W(\mathbf{r}, L)\Phi(\mathbf{q_0}, \mathbf{r}) = \Psi'(\mathbf{q_0}, \mathbf{r})u(\mathbf{r}), \tag{3}$$

where $\Psi'(\mathbf{q_0}, \mathbf{r})$ is equal to $W(\mathbf{r},\ L)\ e^{i\,\mathbf{q_0}\,\mathbf{r}}$. The confined phonon can be described by a wave packet. To calculate the Raman spectrum, one should expand $\Psi'(\mathbf{q_0}, \mathbf{r})$ in a Fourier presentation:

$$\Psi'(\mathbf{q_0}, \mathbf{r}) = \int C(\mathbf{q_0}, \mathbf{q})\ e^{i\,\mathbf{q}\,\mathbf{r}}\ d^3\mathbf{q}. \tag{4}$$

The main task is the determination of Fourier coefficients $C(\mathbf{q_0}, \mathbf{q})$ from an adequate physical model. The "weight" of the phonon with quasi-momentum $\hbar\mathbf{q}$ in the wave packet is proportional to $|C(\mathbf{q_0}, \mathbf{q})|^2$.

The wavenumber of scattered photon is in our case about three orders of magnitude lower than the wavenumber of a phonon at the Brillouin zone boundary, so one can assume $\mathbf{q_0} \cong 0$. So, the first-order Raman spectrum is

$$I(\omega) \cong \int |C(0, \ \mathbf{q})|^2 \frac{n(\omega'(\mathbf{q})) + 1}{(\omega - \omega'(\mathbf{q}))^2 + (\Gamma/2)^2} d^3\mathbf{q} \tag{5}$$

where $n(\omega'(q)) + 1 = \frac{1}{e^{\hbar\omega'(q)/kT} - 1} + 1$ is the Bose-Einstein factor, $\omega'(\mathbf{q})$ is phonon dispersion, and Γ is FWHM of the Raman peak of a single phonon [12–14]. We also have taken into account that the vibration modes (phonons) with lower frequencies have higher amplitudes of vibration. Energy of vibration $\hbar\omega'$ is proportional to $\langle u^2 \rangle k$, where $\langle u^2 \rangle$ is standard deviation of an atom from equilibrium position k which is Hooke's coefficient for a bond, and $k = m\omega'^2$ (m is mass of an atom). So, one can derive $\langle u^2 \rangle \sim \hbar/\omega'$ (Eq. (2.26) in book [15]). This correction is substantial especially for phonons with large frequency dispersion, so we use the equation

$$I(\omega) \cong \int_0^1 |C(0, \mathbf{q})|^2 \frac{n(\omega'(\mathbf{q})) + 1}{\omega'(\mathbf{q}) \cdot \left((\omega - \omega'(\mathbf{q}))^2 + (\Gamma/2)^2\right)} d^3\mathbf{q} \tag{6}$$

It was shown [14] that using a Gaussian curve as eigenfunction for a confined phonon leads to more adequate results than experimental spectra.

Usually, it can be assumed that NCs have a spherical shape with diameter *L*. Therefore, in spherical coordinate system, the phonon weighting function $W(\mathbf{r}, \ L)$ depends only on radius coordinate *r* and does not depend on angles. Assuming that at the boundary of NC (*r* = *L*/2) the phonon amplitude is equal to *1/e* (the phonon amplitude at center of NC is equal to 1), one can obtain.

$$W(\mathbf{r}, L) = \exp\left(-4r^2/L^2\right), \text{so } C(0, \mathbf{q}) \cong \exp\left(-\frac{|\mathbf{q}|^2 L^2}{16}\right) |C(0, q)|^2 \cong \exp\left(-\frac{q^2 L^2}{8}\right) \tag{7}$$

Usually, only empirical expressions for phonon dispersion were used in PCM [12, 13]. But the empirical expressions are accurate enough only near the Brillouin zone center. Also, in earlier approaches, the differences between dispersions of longitudinal optic (LO) and transverse optic (TO) phonons were usually not taken into account. In general, for crystals with diamond-type lattice, there are six phonon branches with dispersions $\omega_i'(q)$, so the first-order Raman spectrum for phonon weighting function $W(\mathbf{r}, \ L) = \exp\left(-4r^2/L^2\right)$ is

$$I(\omega) \cong \sum_{i=1}^{6} \int_0^{q\max} \exp\left(-\frac{q^2 L^2}{8}\right) \frac{n(\omega_i'(q)) + 1}{\omega_i'(\mathrm{q}) \cdot \left((\omega - \omega_i'(\mathrm{q}))^2 + (\Gamma/2)^2\right)} q^2 dq. \tag{8}$$

Wavenumbers are varied from 0 up to q_{max} (edge of the Brillouin zone). For directions with high symmetry (<100> and <111>), it should be noted that some phonon branches are degenerated. The density of states for phonons is proportional to $q^2 dq$.

In some approaches, the phonon frequencies are determined using "ab initio" quantum mechanical calculations [16], but this method requires large computational resources, while NCs with diameters >3 nm contain more than 1 thousand atoms. So, for calculation of phonon dispersion, the Keating model of

valence forces [17] was used. In this simple but adequate model, the elastic energy of the crystal depends on bond length and on deviation of bond angle from ideal tetrahedral angles. We consider atom-atom interaction only between the nearest neighbor. For a crystal with diamond-type lattice, the elastic energy of unit cell is

$$E = \frac{3}{16}\sum_i \sum_j \frac{k_l}{a^2}\left(\left(\vec{r}_i - \vec{r}_j\right)^2 - \frac{3a^2}{16}\right)^2 + \frac{3}{8}\sum_i \sum_{k,j>k}^{4} \frac{k_\varphi}{a^2}\left(\left(\vec{r}_i - \vec{r}_j\right)\cdot\left(\vec{r}_i - \vec{r}_k\right) + \frac{a^2}{16}\right)^2\Bigg], \quad (9)$$

where k_l and k_ϕ are elastic constants (Hooke's coefficients) and a is lattice constant. TO and LO phonons at the Brillouin zone center are degenerated for crystals with diamond-type lattice. The frequency is given by

$$\omega_\Gamma = \sqrt{\frac{8\left(k_l + 3k_\varphi\right)}{3m}} \quad (10)$$

where m is the mass of Ge atoms. As it was mentioned above, Si frequency of TO and LO phonons at the Brillouin zone center is equal to 520.5 cm^{-1}. So, the elastic constants k_ϕ and k_l are not independent [see Eq. (10)]. The elastic constant k_l was determined from approximation of calculated dispersions in directions <100>, <110>, and <111>, obtained from neutron scattering data [18, 19]. It is important to consider phonons of different directions, because in experiment, Raman signal comes from a large amount of randomly oriented NCs, and all phonon modes are intermixed. The exact expressions for phonon dispersions in directions <100>, <110>, and <111> for Keating model are published in Ref. [14] and are very cumbersome. To calculate the first-order Raman spectrum, one should use these dispersions in the Eq. (8). Dispersion in different directions should be used with its corresponding weight. There are 6 physically equivalent <100> directions, so the weight of this dispersion is 6. Similarly the weight of dispersion along <111> and <110> directions are, respectively, equal to 8 and 12. Thus, all calculations were performed with the phonon dispersion in the Keating model, taking into account the phonon dispersion for the three main directions in Si.

Figure 1 shows the results of calculations of the Raman spectra of Si NCs of different diameters using improved PCM. It is seen that for Si NC with diameter of 10 nm, the effect of phonon confinement is significant. The peak shifted and broadened relative to the peak from the bulk Si. For sizes below 10 nm, the NCs' Raman spectrum becomes asymmetric.

Figures 2 and **3** summarize the results of calculations compared with experimental results. **Figure 2** shows the difference between the position of Raman peaks of Si NCs and bulk Si. The average sizes of the Si NCs were determined from HRTEM data. As can be seen, the results of calculations in improved PCM agree well with experimental data but have some differences from the simulation results presented in earlier works [12, 13, 16]. It should be noted that results of calculations in the improved PCM are adequate for a broad range of Si NCs' sizes (from 3 to 10 nm). Note, however, that if during measurements, the heating of the sample under laser spot takes place, the Raman peak will shift (due to anharmonicity of phonons). If the system contains mechanical stress, it will also cause a shift of the Raman peak [14]. **Figure 3** shows the dependence of the Raman peak width with the size of the NCs, for calculation with improved PCM and for experimental data. Some differences between the experimental data and calculations are visible. In particular, large width of the experimental spectra, compared with the calculated spectra, may be due to the dispersion of the size of the Si NCs. Thus, if anharmonicity effect due to heating or mechanical stress is not relevant, the present

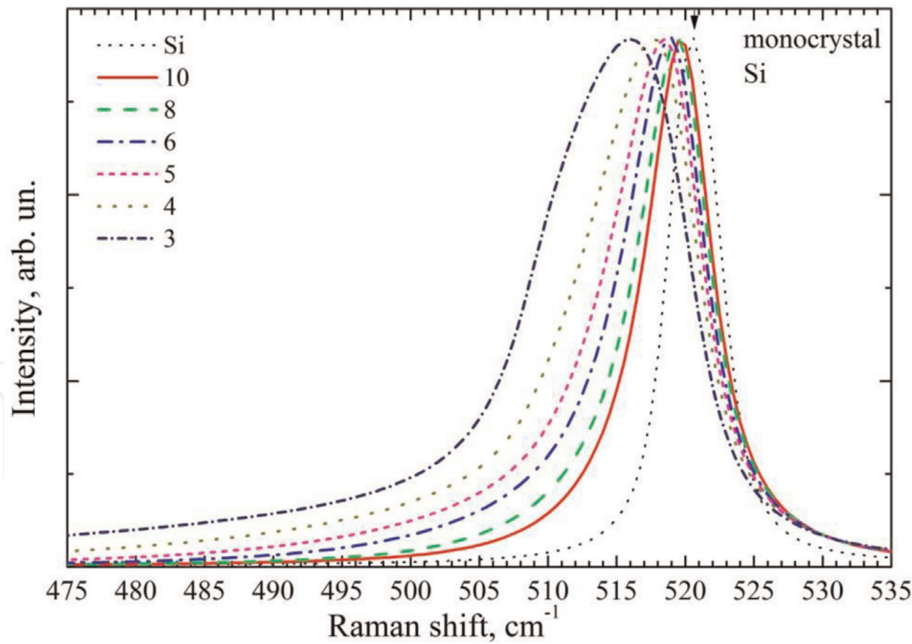

Figure 1.
Calculated Raman spectra of Si NCs of diameters from 10 to 3 nm.

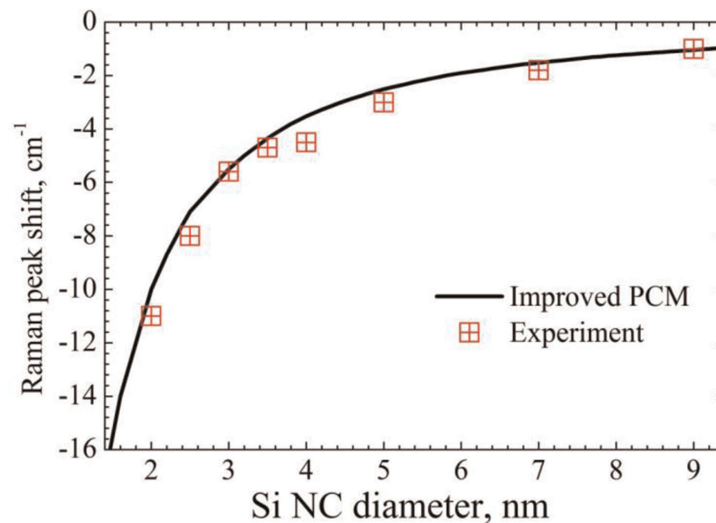

Figure 2.
Shift of the position of the Raman peak for optical phonons confined in Si NCs of various sizes is shown relative to position of Raman peak for bulk Si. The solid curve represents the results obtained using improved PCM (dispersion is calculated in the Keating model taking into account the angular phonon dispersion); red crosses show the experimental data.

improved model allows us to determine the average size of the Si NCs from the analysis of the Raman spectra for a wide range of sizes.

Experimental data on **Figures 2** and **3** were obtained for Si NCs in SiO_x, SiN_x, and amorphous Si matrix and also for free-standing Si nanopowders. This indicates that the PCM is adequate for various matrices; the main demand is that localized phonons in NCs strongly damp in matrix.

In **Figure 4** the Raman spectra of PECVD-deposited SiO_x:H films are shown. Deposition was made from the mixture of monosilane (SiH_4) diluted by argon (Ar) and oxygen (O_2) diluted by helium (He). The stoichiometry parameter “x” was changed by varying of oxygen concentration. The temperature of Si (100) monocrystalline substrate was 200°C. The thickness of SiO_x:H films was about 200 nm. The value of stoichiometry parameter “x” was obtained from the analysis of X-ray photoelectron spectroscopy (XPS) data.

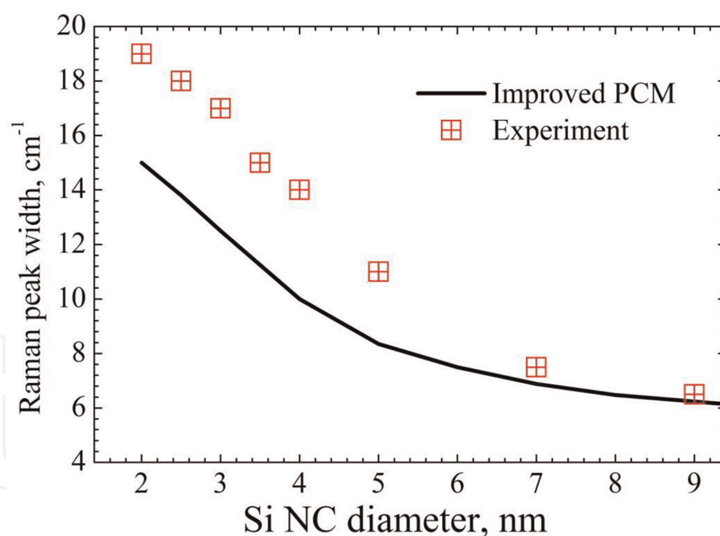

Figure 3.
Width of the Raman peak for optical phonons confined in Si NCs of various sizes. The solid curve represents the results of calculation; red crosses show the experimental data.

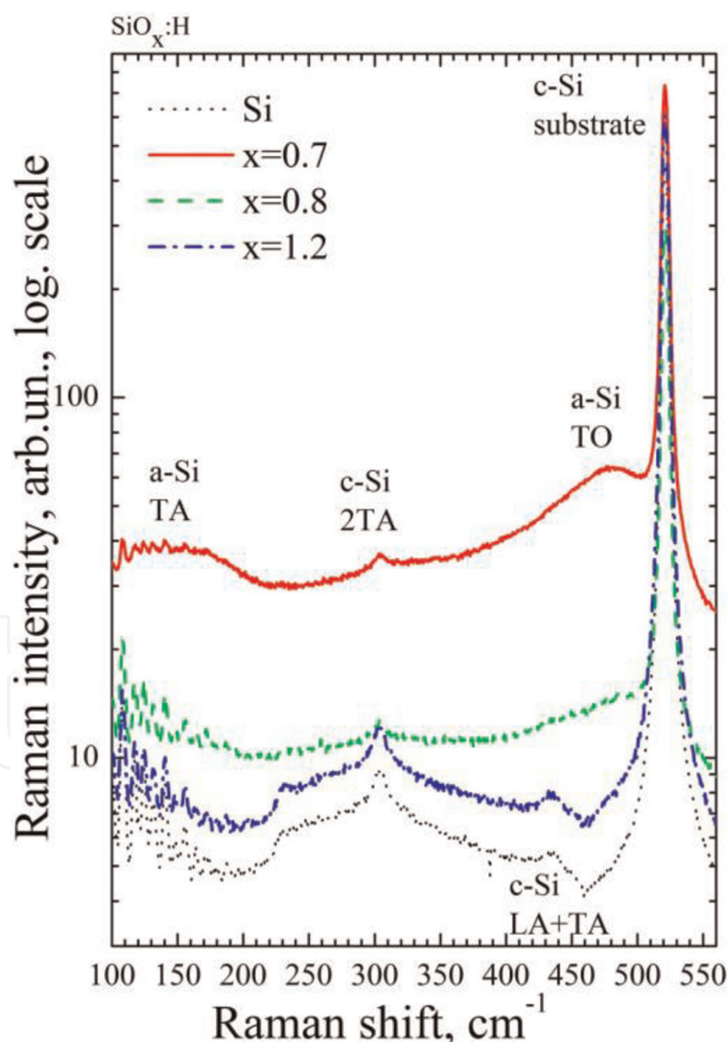

Figure 4.
Raman spectra of SiO_x:H films of different stoichiometry.

Raman spectra were registered at room temperature in back-scattering geometry. For excitation, the 514.5-nm line of an Ar^+ laser was used. No polarization analysis for scattered light was performed. A Horiba Jobin Yvon T64000 spectrometer was used for measuring Raman spectra with a spectral resolution better

than 2 cm^{-1}. A special facility for microscopic Raman studies was also employed. The laser-beam power reaching the sample was 2 mW. For minimization of the heating of the structures under the laser beam, the sample was placed somewhat below the focus in a situation in which the laser-spot size was equal to 10 μm.

So, registered Raman spectra of the SiO_x:H films and the Raman spectrum of a monocrystalline silicon substrate are shown in **Figure 4**. Evidently, a very intense signal due to silicon substrate is observed; this is a line due to the 520.5 cm^{-1} long-wave optical phonon. For clarity, the vertical scale is plotted logarithmic. Besides, features originating from two-phonon scattering phenomena, namely, those due to events involving two acoustic phonons (2TA ~300 cm^{-1}, LA + TA ~425 cm^{-1}), were observed in the spectrum of single-crystal silicon. SiO_x:H films are semitransparent ones in the visible light, and their spectrum also exhibits a signal due to the substrate. The narrow peaks with wavenumbers lower than 160 cm^{-1} resulted from the inelastic scattering of light by atmospheric molecules. As it was mentioned, in Raman spectrum of amorphous Si clusters, there are TO (480 cm^{-1})- and TA (150 cm^{-1})-related broad peaks.

In **Figure 4** one can see that the SiO_x:H films with $x < 1$ contain noticeable amount of amorphous Si clusters. In the spectrum of film with x = 1.2, the TO and TA peaks are practically absent. If the structure of this film corresponded to the RM model, then a significant number of clusters of amorphous silicon would be present in it.

A similar picture is observed for PECVD-grown SiN_x:H films (**Figure 5a**).

The studied SiN_x:H films of different stoichiometric composition were grown using PECVD from a mixture of ammonia (NH_3) and monosilane (SiH_4) on Si substrates with orientation (001). It is known that the composition of SiN_x films ($0 < x < 4/3$) depends on the NH_3/SiH_4 flow ratio. The temperature of the substrates during deposition was 150°C. The value of stoichiometry parameter "x" was defined using of XPS data.

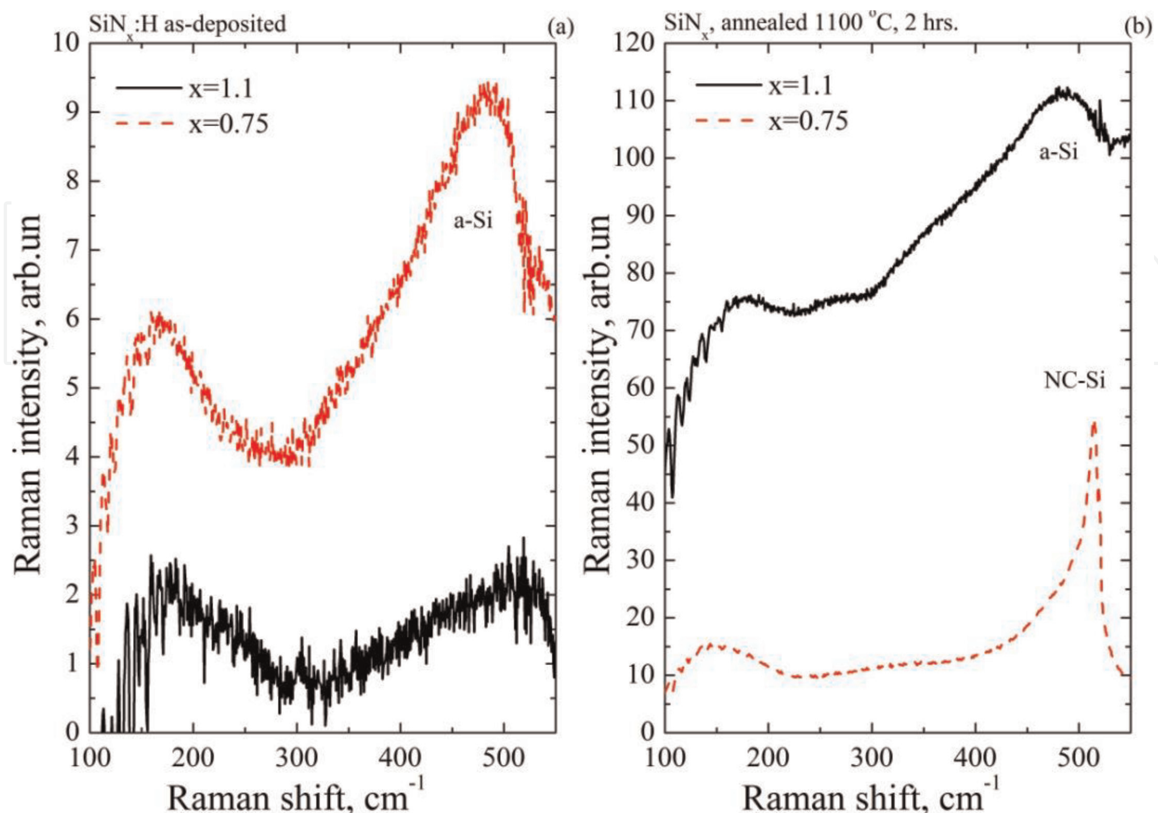

Figure 5.
Raman spectra of SiN_x:H films of different stoichiometry: (a) as-deposited films and (b) as-annealed films.

One can see in Raman spectra of as-deposited SiN_x:H films the amorphous Si peaks (**Figure 5a**). It should be noted that the spectrum of Si substrate was subtracted from spectra of studied structures. One can see that the SiN_x:H films with $x < 1$ contain noticeable amount of amorphous Si clusters. In the as-deposited sample with x = 1.1, the signal from amorphous Si is present, but small.

In **Figure 5b** the spectra of SiN_x films after annealing at Ar atmosphere (1100°C, 2 hours) are presented. One can see that in spectrum of sample with low concentration of Si (x = 1.1), the annealing leads to growth of TO and TA peaks related to amorphous Si. It means that the annealing contributed to the gathering of excess silicon atoms into amorphous clusters and the structure of annealed film is close to RM model. Nevertheless, even such a high-temperature annealing did not lead to crystallization of amorphous nanoclusters. In spectrum of $SiN_{0.75}$ film, there is narrower peak with position 514.5 cm^{-1}. The shift compared with position of peak of monocrystalline Si is about 6 cm^{-1}. According to the data presented in **Figure 2**, such shift is corresponding to Raman scattering by optical phonons localized in Si NCs with average size about 3 nm. It is worth to note that this size is closed to critical size of stable crystalline nuclei of Si.

The photoluminescence under excitation with ultraviolet laser HeCd laser (λ = 325 nm) was also studied in as-deposited and annealed SiN_x:H films. Annealing leads to an increase in the intensity of the photoluminescence, apparently due to the annealing of non-radiative defects. The maximum of the photoluminescence signal shifted to the long-wavelength direction (redshift) with an increase in the content of excess silicon in silicon nitride films.

4. IR absorption in SiO_x and SiN_x films: the evidence of deviation from the RM model

The SiO_x:H and SiN_x:H films were studied using Fourier transform infrared (FTIR) absorption spectroscopy; the spectrometer FT-801 having a spectral resolution of 4 cm^{-1} was used.

The IR spectra of SiO_x samples in **Figure 6** show an absorption peak on the stretching vibrations of the Si—O bonds (TO_3 peak [20]). Pai et al. [21] found that the position of this peak (in inverse centimeters) in SiO_x films almost linearly depends on the stoichiometry parameter x, like.

$$\nu = 925 + 75x \tag{11}$$

From the data of **Figure 6**, it can be seen that the position of the TO_3 peak for the studied samples varies from 1040 to 1060 cm^{-1}. So, according to Eq. (11), the expected stoichiometry of silicon oxide SiO_x should change only slightly. But, according to XPS data, the stoichiometry of the SiO_x films varies widely (from 0.7 to 1.2). This suggests that the structure of our films does not correspond to the RB model (otherwise, the shift range of the TO_3 peak position would be much wider). However, the structure of our films does not correspond to the RM model either (the position of the TO_3 peak for all the films would correspond to the SiO_2 matrix and would be about 1075 cm^{-1}). It is worth also to note that the peaks corresponding to absorption by Si—H and O—H bonds were observed in the films, so the as-deposited SiO_x films are hydrogenated.

Figure 7a shows the IR absorption spectra of as-deposited SiN_x:H films as well as silicon substrate. Nonpolar Si—Si bonds that are active in the Raman process are not active in the absorption process, but Si—N, Si—H, and N—H bonds are active in it, which makes it possible to obtain information on the structure of a-SiN_x:H films

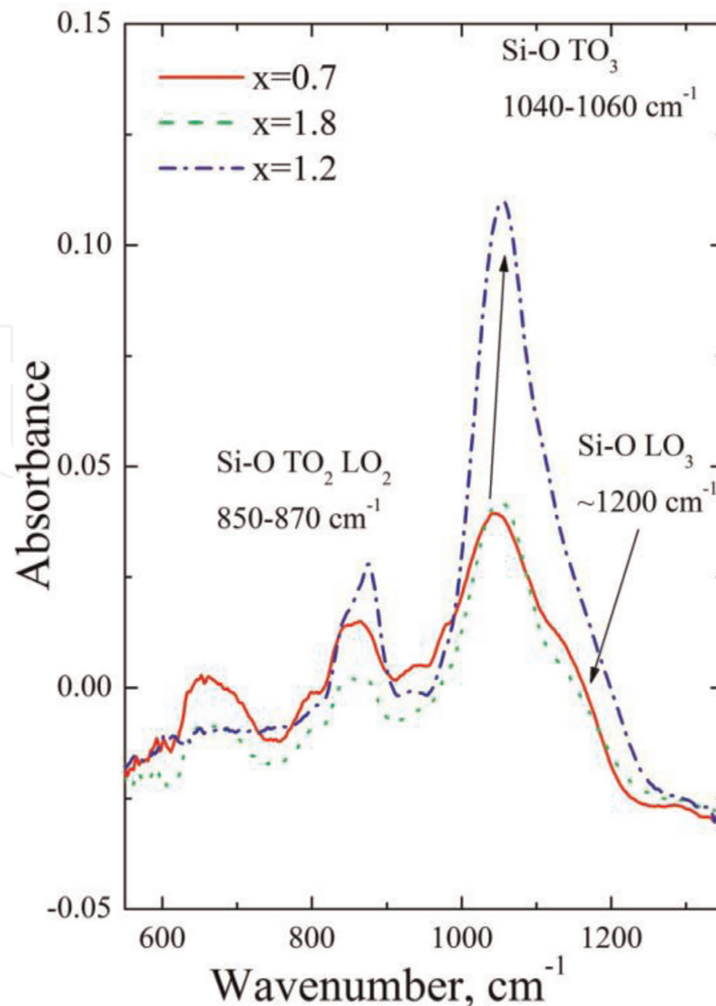

Figure 6.
IR-absorbance spectra of SiO_x:H films of different stoichiometry.

using the IR absorption method. Optical density A (natural logarithm of 1/T, where T is transmission) is plotted on the vertical axis. In the spectra of the films grown at high ratio of ammonia to monosilane fluxes (x = 1.3), absorption peaks at 3340 cm^{-1} are visible. This is the absorption on the stretching vibrations of the nitrogen-hydrogen bonds [22]. In the spectra of the films grown at a ratio of ammonia to monosilane fluxes of 1 and 0.5 (x = 1.1 and 0.75 accordingly), the intensity of this peak is very low, which means that the concentration of hydrogen bound to nitrogen decreases with increasing concentration of excess silicon. It is also seen from **Figure 7** that the spectra of samples containing excess silicon contain a peak with a position of 2150 cm^{-1}. This is the peak from absorption on the stretching vibrations of the silicon-hydrogen bonds [22]. The intensity of this peak depends on the ammonia/monosilane ratio; the intensity is very low in Si_3N_4 film, but it grows with increasing concentration of excess silicon. The peak at ∼1100 cm^{-1} observed in all spectra corresponds to the absorption of stretching vibrations of silicon-oxygen bonds in the silicon substrate. These bonds also give peaks from 400 to 800 cm^{-1} of twisting, wagging, rocking, and scissor modes. In addition, the spectrum of monocrystalline silicon contains peaks from multiphonon lattice absorption in silicon itself (features in the region of 607–614 cm^{-1}). In some spectra, there is also a "parasitic" peak with a position of 2350–2400 cm^{-1} associated with absorption on carbon dioxide gas (in the process of measuring its concentration slightly changed, as a result it was not completely

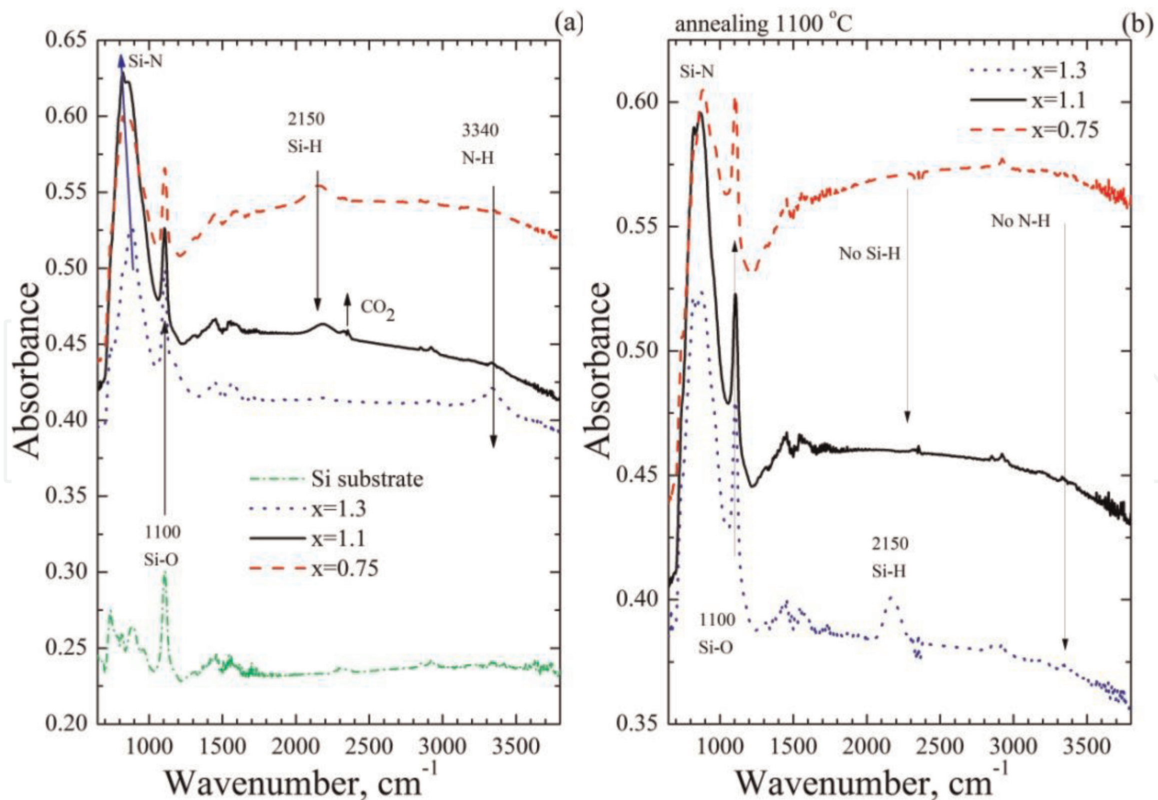

Figure 7.
IR-absorbance spectra of SiN_x:H films of different stoichiometry: (a) as-deposited films and (b) as-annealed films.

removed when dividing the spectrum from the samples by the reference spectrum of the air).

Let us turn to the absorption peak due to vibrations of the Si—N bonds in **Figure 7**. In the spectra of all the films, there are peaks from the stretching vibrations of these bonds. The spectra were approximated by Gaussian curves, and peak positions were determined. The position of the absorption peaks on the stretching vibrations of the Si—N bonds is shifted, depending on the stoichiometry, from 880 to 860 cm^{-1}. This effect was previously known (see work [23] and references therein). The general dependence is that the oscillation frequency decreases with decreasing stoichiometric parameter x in a-SiN_x film. This is observed in our experiment and again confirms that the structure of the films cannot be considered only within the framework of the RM model (in which the stoichiometry of the matrix surrounding the silicon inclusions is unchanged—the matrix parameter x is 4/3).

Figure 7b shows the IR absorption spectra of annealed (Ar atmosphere, 1100°C, 2 hours) SiN_x:H films. One can see that annealing leads to evaporation of hydrogen, except nearly stoichiometry (x = 1.3) film. In that film the Si—H peak becomes even more intensive after annealing. So, hydrogen has been removed from N—H bonds to Si—H bonds. This effect has already been observed in the work [24]. In the work [24], it was shown that in order to remove hydrogen from Si—H bonds, it is necessary to apply high-temperature annealing at very high pressure. It should be noted that in annealed films the position of the absorption peaks on the stretching vibrations of the Si—N bonds is also shifted, depending on the stoichiometry. The lesser parameter x, the higher is frequency of stretching vibrations of the Si—N bonds.

So, the analysis of IR absorption data is an evidence of deviation of structure of real SiO_x and SiN_x films from the RM model.

5. New structural model explaining nanofluctuations of potential in SiO_x and SiN_x

Nonstoichiometric silicon oxide SiO_x and nitride SiN_x are tetrahedral compounds whose structure is defined by the Mott octahedral rule [7, 25]. SiO_x and SiN_x are synthesized under thermodynamically nonequilibrium conditions. Therefore, the structure of nonstoichiometric SiO_x and SiN_x layers depends on synthesis conditions, i.e., temperatures, gas pressure, and annealing.

The RB and RM models [7] are two extreme cases of the SiO_x and SiN_x structure description. As a rule, at low synthesis temperatures (<300°C), its structure is described by the RB model; higher synthesis temperatures promote phase separation in SiO_x layers, i.e., such layers should be better described by the RM model.

According to the RB model [26], the probability of finding the $SiO_vSi_{(4-v)}$ tetrahedron (the fraction of given v-type tetrahedra), where v = 0, 1, 2, 3, 4 in SiO_x for composition x, is given by.

$$W_\nu^{RB}(x) = \frac{4!}{\nu!(4-\nu)!}\left(\frac{x}{2}\right)^\nu \left(1-\frac{x}{2}\right)^{4-\nu} \tag{12}$$

According to the RM model [7], the calculated spectrum consists of two tetrahedron types, SiO_4 and $SiSi_4$. The fraction of SiO_4 and $SiSi_4$ tetrahedra in the calculation of Si 2p spectra is (1 − x/2) and x/2, respectively. To simulate the photoelectron spectrum *I(E)*, the W_v peaks obtained using the RB and RM models were broadened by the Gaussian using the formula:

$$I(E) = \sum_\nu W_\nu e^{-(E-E_\nu)^2/2\sigma_\nu^2} \tag{13}$$

where E_v and σ_v are the peak energy and "half-width" for a given tetrahedron type. The SiO_x film composition was calculated assuming that the calculated spectrum is a superposition of five peaks corresponding to five $SiO_vSi_{(4-v)}$ tetrahedra, v = 0, 1, 2, 3, 4. The fraction of tetrahedral was selected from the best fit of the spectrum *I(E)* calculated by Formula (12).

Figure 8a shows five experimental photoelectron spectra of the Si 2p level in SiO_x. We can see that the energy and half-width of the Si_{4+} peak belonging to the a-SiO_2 phase and the Si peak belonging to the a-Si phase are E_0 = 103.5 eV and σ_0 = 1.2 eV and E_4 = 99.5 eV and σ_4 = 0.6 eV, respectively. The position and half-width for Si_{3+}, Si_{2+}, and Si_+ peaks ($SiSiO_3$, $SiSi_2O_2$, and $SiSi_3O$ tetrahedra) were determined using linear interpolation of E_0, E_4, σ_0, and σ_4 using the number of oxygen atoms as a parameter. Dashed curves in **Figure 8a** show the spectra calculated from the best fit with experimental spectra. The calculation for the SiO_x film composition predicts the following values, x = 0, 0.7, 0.98, 1.47, and 2.0.

Figure 8b shows the experimental photoelectron spectra of the Si 2p level in SiO_x and the results of RB model simulation. The RB model predicts a single peak being a superposition of five peaks corresponding to five $SiO_vSi_{(4-v)}$ tetrahedra (v = 0, 1, 2, 3, 4). The calculated peak shifts to lower binding energies with decreasing oxygen concentrations. The position and half-width of the calculated SiO_x peak for x = 0.7, 0.98, 1.47 is not in agreement with the experimental spectrum

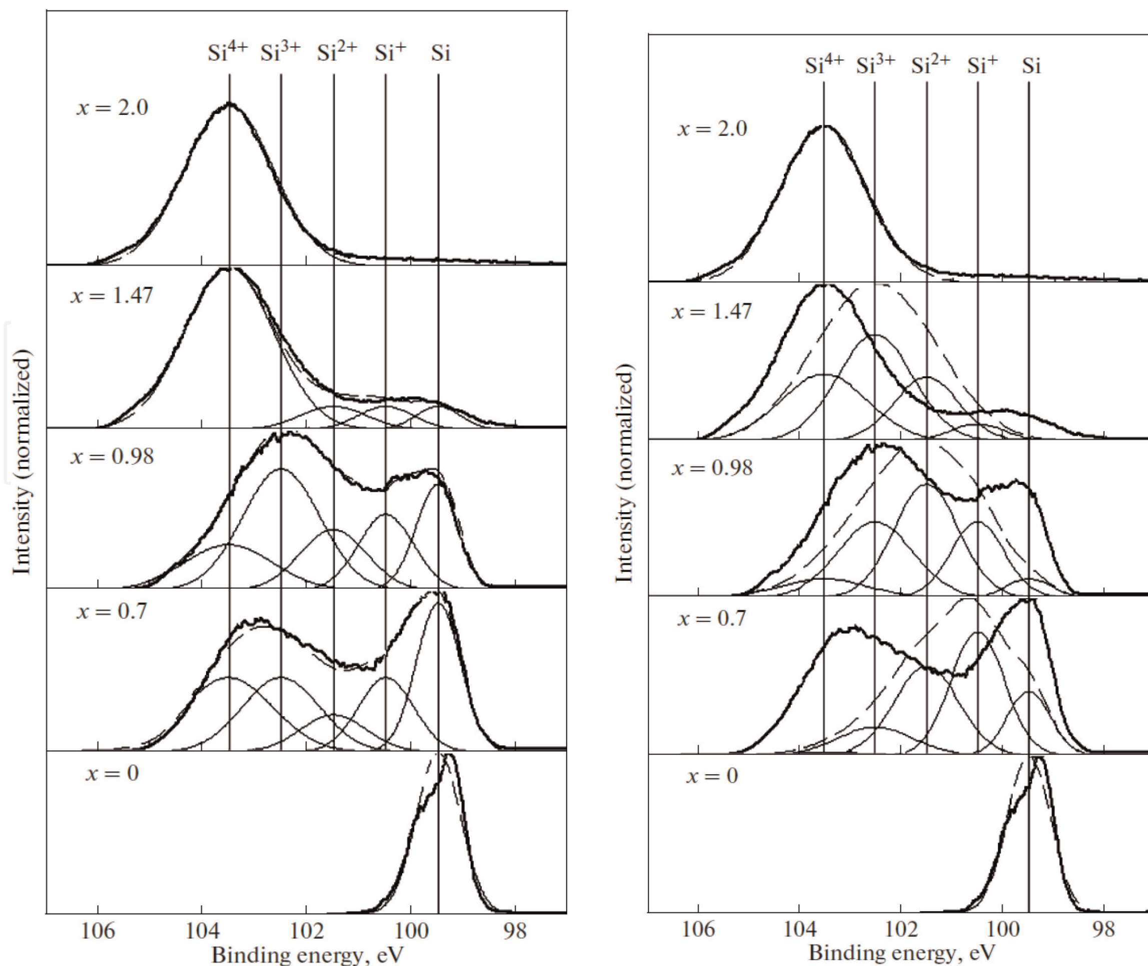

Figure 8.
(a) (left) Experimental photoelectron spectra of the Si 2p level in SiO_x (bold curve) and simulation results for determining the film composition (dashed curve). Symbols Si_{4+}, Si_{3+}, Si_{2+}, Si, and Si indicate intensities of the Si 2p level for SiO_4, $SiSiO_3$, $SiSi_2O_2$, $SiSi_3O$, and $SiSi_4$ tetrahedra, respectively. (b) (right) Experimental photoelectron spectra of the Si 2p level in SiO_x (bold curve) and the results of simulation using the RB model (dashed curve). Symbols Si_{4+}, Si_{3+}, Si_{2+}, Si_{+}, and Si indicate intensities of the Si 2p level for SiO_4, $SiSiO_3$, $SiSi_2O_2$, $SiSi_3O$, and $SiSi_4$ tetrahedra, respectively.

of the Si 2p level. The RB model underestimates the role of $SiSi_4$ and SiO_4 tetrahedra in calculating the intermediate SiO_x composition (x = 0.7, 0.98, 1.47). Thus, there are five $SiO_vSi_{(4-v)}$ tetrahedron types in SiO_x; however, the probability of their detection is not quantitatively described by the RB model.

The calculation of experimental spectra using the RM model is shown in **Figure 9a**. According to the RM model, the calculation predicts the existence of two peaks corresponding to SiO_4 and $SiSi_4$ tetrahedra. The calculated energies of the Si 2p level peaks correlate with those of experimental spectra. The calculated spectra underestimate the contribution of $SiSiO_3$, $SiSi_2O_2$, and $SiSi_3O$ tetrahedra which exist in experimental spectra. For example, for $SiO_{0.98}$, the calculation predicts the presence of the SiO_2 phase which is not observed in experimental spectra. Thus, the RM model also does not describe the experimental photoelectron spectra.

We note that it is impossible to describe experimental spectra by summing the RB and RM spectra in corresponding proportions. This is easily seen in the case of the composition x = 0.7 for which both RB and RM models predict a significantly smaller content of the SiO_2 phase than it is observed in the experiment.

Figure 9b shows the photoelectron spectra of the valence band of SiO_x of variable composition, measured at an excitation energy of 1486.6 eV. At such an excitation energy, silicon states make the main contribution to the valence band

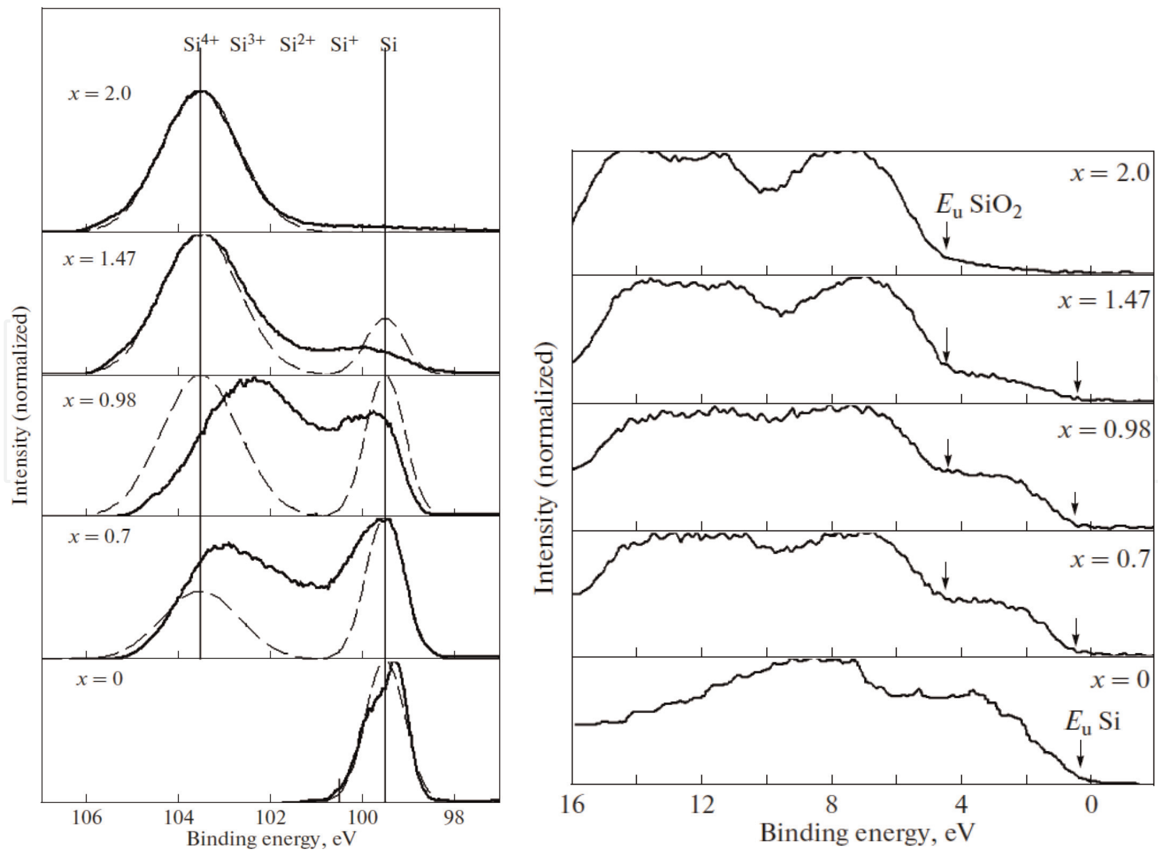

Figure 9.
(a) (left) Experimental photoelectron spectra of the Si 2p level in SiO_x (bold curve) and the results of simulation using the RM model (dashed curve). Symbols Si_{4+} and Si indicate intensities of the Si 2p level for SiO_4 and $SiSi_4$ tetrahedra, respectively. (b) (right) Experimental XPS data of the valence band of SiO_2, SiO_x, and Si. The top of the silicon valence band is taken as the reference point.

spectrum. Oxygen states (O 2p) at such excitation energies make a small contribution due to a low photoionization cross section. The SiO_x ($x > 0$) photoelectron spectrum contains three distinct peaks. As the silicon contents in SiO_x increase above the top of the silicon valence band (E_v Si), states caused by silicon appear (**Figure 9b**). The low-energy peak at 0–4 eV is caused by Si 3p orbitals in amorphous silicon. The peaks at energies above 4 eV are caused by Si 3s and 3p orbitals. These results independently point to the fact that SiO_x contains SiO_2 and Si.

To describe the SiO_x structure, it was proposed to use the intermediate model (IM). The IM model assumes local fluctuations of the SiO_x chemical composition, which result in bandgap fluctuations. For example, in [27], it was shown that the chemical composition of silicon oxide films can be identical, $SiO_{1.94}$, while the bandgap can vary in the range of 5.0–7.5 eV. **Figure 10a** shows the SiO_x energy-level diagram for section *A–A*. The horizontal line ($E = 0$) is electron energy reference point (the energy of vacuum). Symbols E_c and E_v denote the bottom of the conduction band and the top of the valence band in SiO_x. The SiO_2 bandgap is 8 eV [7]. Bandgap narrowing indicates a local increase in the silicon concentration in SiO_x. The least bandgap ($E_g = 1.5$ eV) corresponds to the silicon phase. Thus, the maximum scale of potential fluctuations for electrons and holes is 2.6 and 3.8 eV, respectively. **Figure 10a** shows all possible versions of the SiO_x spatial structure. White, black, and gray colors correspond to SiO_2, a-Si, and silicon suboxides, respectively. If the silicon cluster size *L* is small, size quantization effects can be observed in it. Such a cluster is indicated in the figure by numeral *1*. Numeral *2* indicates the macroscopic silicon cluster in silicon oxide. In this case, the intermediate layer of silicon suboxides is absent, and the Si/SiO_2 interface in the

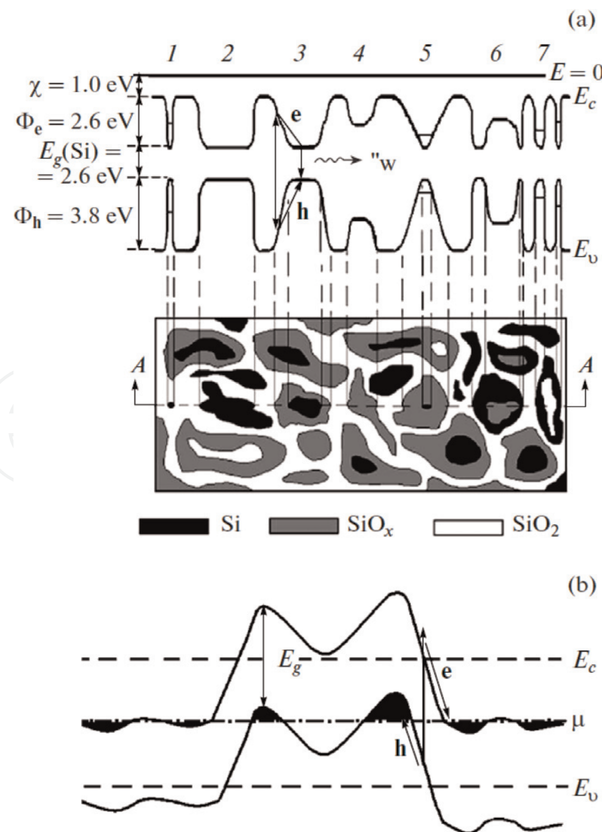

Figure 10.
(a) IM model: the schematic two-dimensional pattern of the SiO_x structure and the SiO_x energy-level diagram for section A–A. White, black, and gray colors correspond to SiO_2, a-Si, and silicon suboxides, respectively. Φ_e and Φ_h barriers for electrons and holes at the interface a-Si/SiO_2, respectively. (b) Model of potential fluctuation (Shklovskii-Efros model) in a heavily doped compensated semiconductor; μ is the Fermi level.

energy-level diagram boundary is sharp. Numeral *3* indicates the silicon cluster surrounded by silicon suboxide. In this case, the Si/SiO_2 interface in the energy-level diagram is shown by a smooth curve. Hereafter, it is assumed that the intermediate region (silicon suboxide) size significantly exceeds the Si—O and Si—Si bond length. Numeral *4* indicated the suboxide silicon cluster in SiO_2. Numeral *5* indicates the silicon cluster in silicon suboxide. Numeral *6* indicates the suboxide cluster in silicon, and numeral *7* indicates the SiO_2 cluster in silicon.

The model of large-scale potential fluctuations (Shklovskii-Efros model) in a heavily doped compensated semiconductor was developed earlier (**Figure 10b**) [28]. In this model, the bandgap is constant, and potential fluctuations occur due to the nonuniform spatial distribution of the charged ionized donors and acceptors. An electron-hole pair excitation results in spatial separation of electrons and holes, which does not facilitate their recombination. The principal difference between the proposed model of nanoscale potential fluctuations in SiO_x and the Shklovskii-Efros model is as follows. Large-scale potential fluctuations in compensated semiconductors are of electrostatic nature associated with spatial fluctuations of the charge density of donors and acceptors. The bandgap is constant (**Figure 10b**), and the electric field caused by spatial potential fluctuations promotes electron and hole separation. In SiO_x, potential fluctuations are caused by local fluctuations of the chemical composition.

In the IM model, in contrast to the Shklovskii-Efros model, the space charge is absent. According to the IM model, local fluctuations in the SiO_x chemical composition result in spatial potential fluctuations which, in turn, lead to changes in local electric fields for electrons and holes. These fields at the same point of the SiO_x sample are different in magnitude and direction (**Figure 10a**). When an

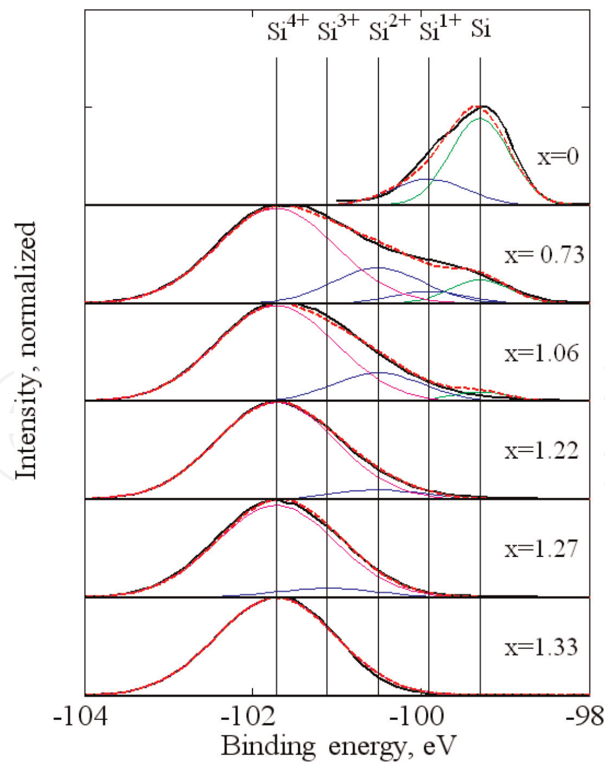

Figure 11.
Experimental XPS spectra of the Si 2p level in SiN_x (solid black lines) and the results of theoretical modeling using the IM model (dashed red lines). Green line is peak from Si—Si_4 tetrahedron, and magenta line is peak from Si—N_4 tetrahedron.

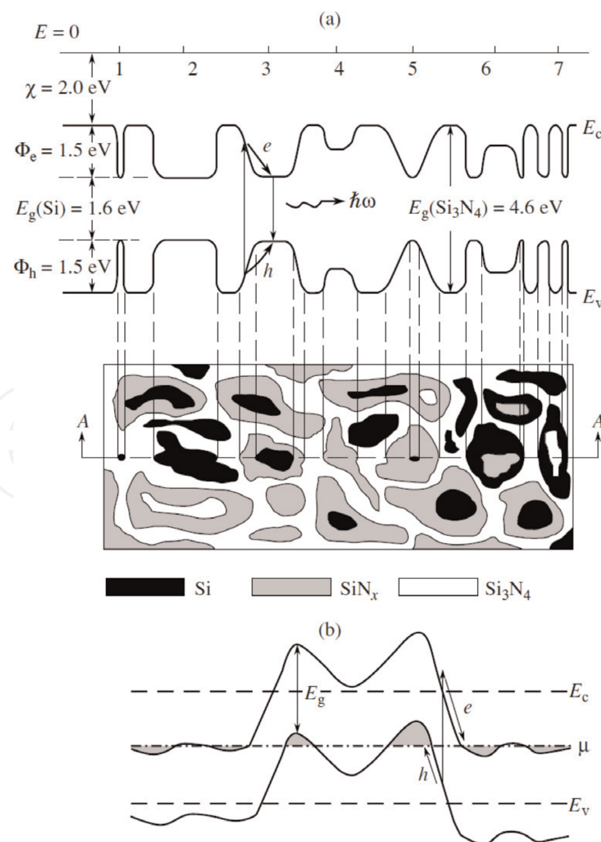

Figure 12.
Schematic diagrams illustrating the proposed intermediate model of SiN_x: (a) a two-dimensional diagram of SiN_x structure showing (bottom) the regions of a silicon phase, stoichiometric silicon nitride, and subnitrides and (top) the energy band profile of SiN_x in the A–A section (E_c is the conduction band bottom; E_v is the valence band top; Φ_e and Φ_h are the energy barriers for electrons and holes at the a-Si–Si_3N_4 interfaces, respectively; E_g is the bandgap width). (b) The potential fluctuations in Shklovskii–Efros model.

electron-hole pair is excited in SiO_x, the electric field for electron and hole promotes (see in **Figure 10a**) their recombination. In the case of the radiative recombination mechanism, SiO_x is an efficient emitting medium. Nanoscale potential fluctuations in SiO_2 promote electron and hole localization in potential wells (silicon clusters) [7]. This effect is used for developing the high-speed nonvolatile memory based on charge localization in SiO_x and can be used in memristors.

In the case of SiN_x films, the approach for determining the stoichiometric parameter x from XPS data analysis is similar, but unlike Eq. (12), the probability of finding the $SiN_vSi_{(4-v)}$ tetrahedron (the fraction of given v-type tetrahedra), where v = 0, 1, 2, 3, 4 in SiN_x for composition x, is given by

$$W_v^{RB}(v,x) = \frac{4!}{v!(4-v)!}\left(\frac{3x}{4}\right)^v\left(1-\frac{3x}{4}\right)^{4-v} \quad (14)$$

Experimental XPS spectra are also not described by pure RB or RM models. However, good agreement between the experimental and calculated spectra is observed for IM model (**Figure 11**).

The nanoscale fluctuations of potential in SiN_x films (**Figure 12**) are also similar to nanoscale fluctuations of potential in SiO_x. In the case of SiN_x films, the IM is more adequate to describe the real structure and fluctuation of potential. In schematic picture in the bottom of **Figure 12**, one can see the possible appearance of such structures—Si core surrounded by SiN_x shell and Si_3N_4 matrix. So, the proposed IM also can be called as core-shell-matrix model.

6. Memristor effects in SiO_x films

Resistive random-access memory (RRAM) [29, 30] is the highly promising candidate for the next-generation nonvolatile memory (NVM), because conventional charge-based memories, namely, dynamic random-access memory and flash memory, have too low capacitance after continuously downscaling into 1X-nm regimes. In addition, an RRAM array can be fabricated in the back end of the line of a complementary metal-oxide-semiconductor circuit, which makes such device an excellent candidate for embedded NVM (e-NVM) application. The typical write speed of RRAM device ranges from 100 ns to 1 μs, which is three to four orders of magnitude faster than flash memory. Such high-speed and process-compatible e-NVM can enable hardware technologies such as artificial intelligence and neuromorphic computing.

The conduction mechanism of RRAM, however, is not fully understood, and it is generally attributed to metallic filament conduction because of its metal-insulator-metal (MIM) structure, where the insulator is usually formed by metal oxide-based dielectric. The first RRAM that does not contain any metal in both the electrodes and dielectric insulator (nonmetal RRAM) is demonstrated here. To obtain RRAM device, a 15-nm-thick SiO_x was deposited directly on a p^+-Si substrate by reactive sputtering. Then, a 15-nm-thick amorphous n^+-Si layer was formed as the top junction electrode. The value x in SiO_x was determined to be 0.62. Because no metal or metallic ions were present in the whole RRAM device, metallic filaments were not formed.

Figure 13(a) depicts the measured *I-V* characteristics of an n^+-Si/$SiO_{0.62}$/p^+-Si RRAM device. During the forming step, the device was first subjected to a 6 V and 100 μA compliance current stress to attain the LRS. The same device was reset into

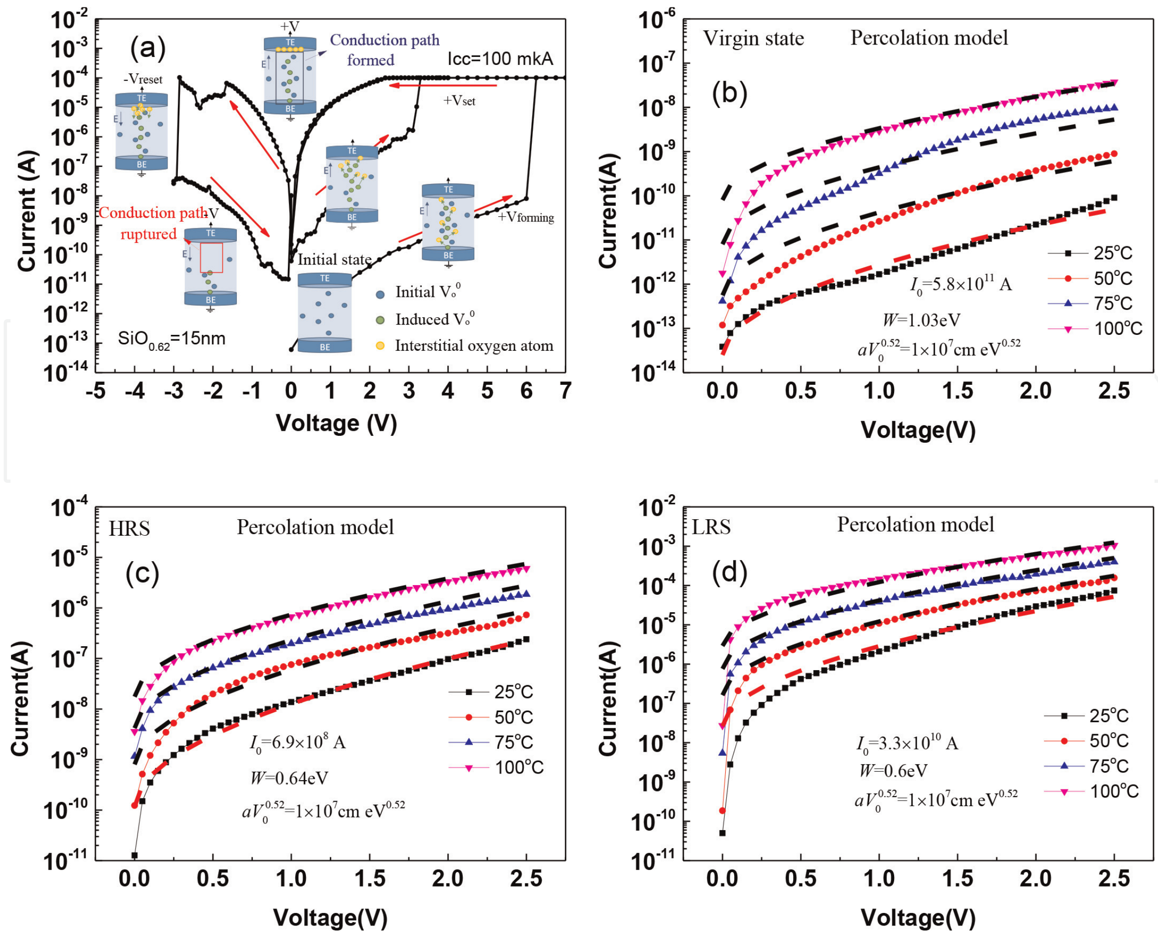

Figure 13.
(a) I-V characteristics of n^+-Si/$SiO_{0.62}$/p^+-Si RRAM device under forming, set, and reset operations. I-V dependences of (b) VS, (c) HRS, and LRS (d) currents of n^+-Si/SiO_x/p^+-Si RRAM and fitting curves of Shklovskii-Efros model.

HRS after a negative voltage bias. Then, the device was set to LRS again under a positive voltage bias. However, the positive set voltage was lower than the forming voltage once the RRAM switching function was established.

The current conduction mechanism is crucial for RRAM devices. To understand the conductive mechanism in this completely nonmetal RRAM, the measured *I-V* curves at different temperatures were further analyzed. **Figure 13(b)**, **(c)**, and **(d)** depict the measured and modeled *I-V* curves in the virgin state (VS), HRS, and LRS conditions, respectively. All state the HRS and LRS currents adhere to the Shklovskii-Efros percolation model [28]:

$$I = I_0 \exp\left(-\frac{W_e - \left(Ce\frac{U}{d}aV_0^{\gamma}\right)^{\frac{1}{1+\gamma}}}{kT}\right) \tag{15}$$

where I_0, W_e, a, V_0, C, and γ are the preexponential factor, percolation energy, space scale of fluctuations, energy fluctuation amplitude, numeric constant which is equal to 0.25, and critical index which is equal to 0.9, respectively. The simulation by the Shklovskii-Efros model gives reasonable model parameters to all resistance state (**Figure 13(b–d)**). The percolation energy decreases with decreasing resistance. The relation $a \times V_0^{0.52} = 1 \times 10^{-7}$ cm $eV^{0.52}$ does not change from resistance to resistance. This is due to the fact that decreasing resistance increases space scale of fluctuations a, but decreases energy fluctuation amplitude V_0. In addition, it can be said that the Shklovskii-Efros percolation model is applicable to the LRS case,

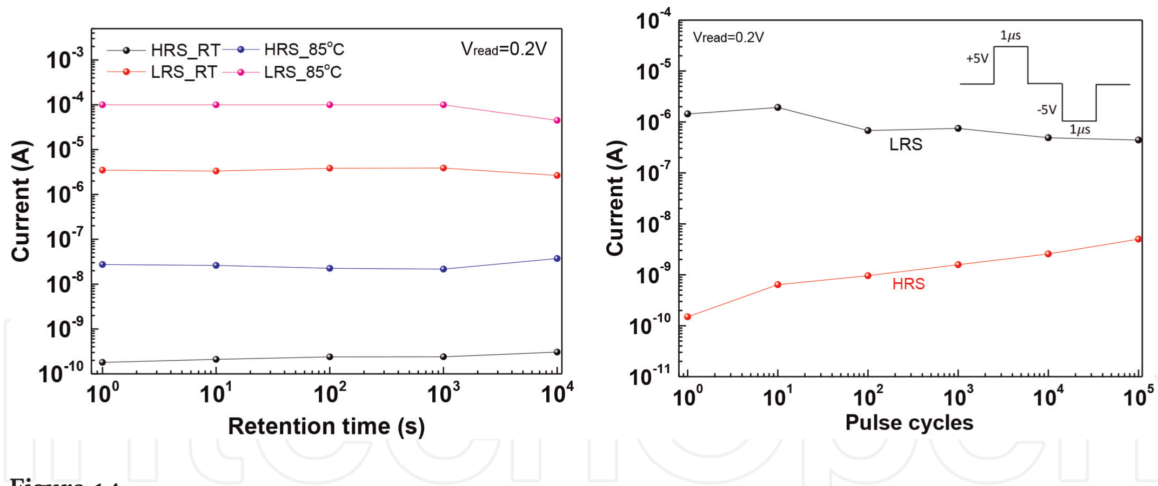

Figure 14.
(left) Retention characteristics of n^+-Si/$SiO_{0.62}$/p^+-Si RRAM devices at RT and 85°C. (right) Endurance characteristics of n^+-Si/$SiO_{0.62}$/p^+-Si RRAM devices.

and then, it can be assumed that the conducting channel is not continuous. Hence, the simulated results demonstrate that the charge transport of the n^+-Si/$SiO_{0.62}$/p^+-Si RRAM in VS, HRS, and LRS are described by the Shklovskii-Efros percolation model.

Figure 13(a) plots potential switching mechanisms. During the forming step, the current is conducted through the initial V_o^{2+} inside the SiO_x layer [31]. When the RRAM device was under sufficiently high positive voltage, soft breakdown in SiO_x occurred and disrupted the covalent bonds [32], generating unbonded Si ions, O^{2-}, and V_o^{2+}. It is assumed that after generation of anti-Frenkel pairs, electrons are redistributed to maintain charge neutrality, and new oxygen vacancies (V_o^0) and interstitial oxygen atoms are formed [30]. Because the atomic size of O is significantly smaller than Si, the interstitial oxygen atoms and V_o^0 could migrate inside SiO_x under the applied electric field. At the end of the forming process, the interstitial oxygen atoms were attracted to the positive voltage and accumulated at the interface of top n^+-i junction. Once the conduction path was formed, electrons could transport through the V_o^0, creating the LRS current pass in the SiO_x layer. After application of a negative voltage, interstitial oxygen atoms moved away from the top n^+-i junction and recombined with V_o^0 to rupture the conduction path—the reset process. After a positive voltage was applied again, the set process behaved as the forming process to form a conduction path, but under a lower positive voltage than the forming voltage due to not all generating in the forming process V_o^0 recombined in the reset process.

Data retention and endurance are necessary characteristics for NVM, and they are related to the nonvolatile behavior and lifetime of an RRAM device. **Figure 14** (left) depicts the retention characteristics of the n^+-Si/$SiO_{0.62}$/p^+-Si RRAM device. The completely nonmetal RRAM device could achieve favorable retention with a slight resistive window decay from 1.9×10^4 to 8.7×10^3 at RT and 3.6×10^3 to 1.2×10^3 at 85°C after 10^4 s retention.

Figure 14 (right) depicts the pulsed endurance of the n^+-Si/$SiO_{0.62}$/p^+-Si RRAM device under set/reset pulses of +5/−5 V for 1 μs. In this case, higher voltages were used than DC switching cases because the energy to disrupt the covalent SiO_x bonds equals to the multiplication of *I, V,* and *time*. The resistance ratio between HRS and LRS decreased after increasing the pulsed cycles; however, the device exhibited excellent endurance with a resistance window of 89 after 10^5 pulsed switching cycles [33].

7. Conclusions

The silicon amorphous nanoclusters in as-deposited SiO_x and SiN_x films and silicon nanocrystals in the annealed films were studied using structural and optical methods. To analyze the sizes of silicon nanocrystals from the analysis of Raman scattering data, the phonon confinement model was refined.

From the analysis of XPS, Raman, and IR spectroscopy data, it has been established that pure random mixture and random bonding models do not adequately describe the real structure of the SiO_x and SiN_x films. The intermediate model was proposed. The nanoscale potential fluctuations in SiO_x and SiN_x films can be interpreted in the framework of the proposed model. The memristor effects in SiOx-based nonmetal structures were demonstrated.

Acknowledgements

The work was supported by the Russian Science Foundation (Project No. 18-49-08001) and the Ministry of Science and Technology (MOST) of Taiwan (No. 107-2923-E-009-001-MY3).

Author details

Vladimir Volodin[1,2*], Vladimir Gritsenko[1,2,3], Andrei Gismatulin[1] and Albert Chin[4]

1 Rzhanov Institute of Semiconductor Physics SB RAS, Novosibirsk, Russia

2 Novosibirsk State University, Novosibirsk, Russia

3 Novosibirsk State Technical University, Novosibirsk, Russia

4 National Chiao Tung University, Hsinchu, Taiwan, ROC

*Address all correspondence to: volodin@isp.nsc.ru

IntechOpen

© 2019 The Author(s). Licensee IntechOpen. This chapter is distributed under the terms of the Creative Commons Attribution License (http://creativecommons.org/licenses/by/3.0), which permits unrestricted use, distribution, and reproduction in any medium, provided the original work is properly cited.

References

[1] Pavesi L, Turan R, editors. Silicon Nanocrystals Fundamentals, Synthesis and Applications. Germany: Wiley; 2010. p. 652. ISBN: 978-3-527-32160-5

[2] Greben M, Khoroshyy P, Liu X, Pi X, Valenta J. Fully radiative relaxation of silicon nanocrystals in colloidal ensemble revealed by advanced treatment of decay kinetics. Journal of Applied Physics. 2017;**122**:034304. DOI: 10.1063/1.4993584

[3] Sychugov I, Juhasz R, Valenta J, Linnros J. Narrow luminescence linewidth of a silicon quantum dot. Physical Review Letters. 2005;**94**: 087405. DOI: 10.1103/PhysRevLett. 94.087405

[4] Park N-M, Kim T-S, Park S-J. Band gap engineering of amorphous silicon quantum dots for light-emitting diodes. Applied Physics Letters. 2001;**78**:2575-2577. DOI: 10.1063/1.1367277

[5] Anutgan T, Anutgan M, Atilgan I, Katircioglu B. Electroformed silicon nitride based light emitting memory device. Applied Physics Letters. 2017;**111**:053502. DOI: 10.1063/ 1.4997029

[6] Gismatulin AA, Kruchinin VN, Gritsenko VA, Prosvirin IP, Yen T-J, Chin A. Charge transport mechanism of high-resistive state in RRAM based on SiO_x. Applied Physics Letters. 2019;**114**: 033503. DOI: 10.1063/1.5074116

[7] Gritsenko VA. Atomic structure of amorphous nonstoichiometric silicon oxides and nitrides. Physics-Uspekhi. 2008;**178**:699-708. DOI: 10.1070/ PU2008v051n07ABEH006592

[8] Smith JE Jr, Brodsky MH, Crowder BI, Nathan MI. Raman spectra of amorphous Si and related tetrahedrally bonded semiconductors. Physical Review Letters. 1971;**26**:642-646. DOI: 10.1103/PhysRevLett.26.642

[9] Parker JH Jr, Feldman DW, Ashkin M. Raman scattering by silicon and germanium. Physical Review. 1967;**155**: 712-714. DOI: 10.1103/PhysRev.155.712

[10] Bustarret E, Hachicha MA, Brunel M. Experimental determination of the nanocrystalline volume fraction in silicon thin films from Raman spectroscopy. Applied Physics Letters. 1988;**52**:1675-1677. DOI: 10.1063/ 1.99054

[11] Zhigunov DM, Kamaev GN, Kashkarov PK, Volodin VA. On Raman scattering cross section ratio of crystalline and microcrystalline to amorphous silicon. Applied Physics Letters. 2018;**113**:023101. DOI: 10.1063/ 1.5037008

[12] Richter H, Wang ZP, Lay L. The one phonon Raman spectrum of microcrystalline silicon. Solid State Communications. 1981;**39**:625-629. DOI: 10.1016/0038-1098(81)90337-9

[13] Pailard V, Puech P, Laguna MA, Carles R, Kohn B, Huisken F. Improved one-phonon confinement model for an accurate size determination of silicon nanocrystals. Journal of Applied Physics. 1999;**86**:1921-1924. DOI: 10.1063/1.370988

[14] Volodin VA, Sachkov VA. Improved model of optical phonon confinement in silicon nanocrystals. Journal of Experimental and Theoretical Physics. 2013;**116**:87-94. DOI: 10.1134/ S1063776112130183

[15] Cardona M, Günterodt G, editors. Light Scattering in Solids II. Basic Concept and Instrumentation. Berlin: Springer-Verlag; 1982. p. 251. ISBN: 3-540-11380-0

[16] Cheng W, Ren S-F. Calculations on the size effects of Raman intensities of silicon quantum dots. Physical Review B. 2002;**65**:205305. DOI: 10.1103/PhysRevB.65.205305

[17] Keating PN. Effect of invariance requirements on the elastic strain energy of crystals with application to the diamond structure. Physics Review. 1966;**145**:637-645. DOI: 10.1103/PhysRev.145.637

[18] Dolling G. Lattice vibrations in crystals with the diamond structure. In: Inelastic Scattering of Neutrons in Solids and Liquids: II. Proceedings of IAEA, Vienna. 1963. pp. 37-48

[19] Kulda J, Strauch D, Pavone P, Ishii Y. Inelastic-neutron-scattering study of phonon eigenvectors and frequencies in Si. Physical Review B. 1994;**50**:13347-13356. DOI: 10.1103/PhysRevB.50.13347

[20] Kirk CT. Quantitative analysis of the effect of disorder-induced mode coupling on infrared absorption in silica. Physical Review B. 1988;**38**:1255-1273. DOI: 10.1103/PhysRevB.38.1255

[21] Pai PG, Chao SS, Takagi Y, Lucovsky G. Infrared spectroscopic study of SiO_x films produced by plasma enhanced chemical vapor deposition. Journal of Vacuum Science and Technology A. 1986;**4**:689-694. DOI: 10.1116/1.573833

[22] Yin Z, Smith FW. Optical dielectric function and infrared absorption of hydrogenated amorphous silicon nitride films: Experimental results and effective-medium-approximation analysis. Physical Review B. 1990;**42**:3666-3675. DOI: 10.1103/PhysRevB.42.3666

[23] Korchagina TT, Marin DV, Volodin VA, Popov AA, Vergnat M. Structure and optical properties of SiN_x: H films with Si nanoclusters produced by low frequency plasma enhanced chemical vapor deposition. Semiconductors. 2009;**43**:1514-1520. DOI: 10.1134/S1063782609110207

[24] Volodin VA, Bugaev KO, Gutakovsky AK, Fedina LI, Neklyudova MA, Latyshev AV, et al. Evolution of silicon nanoclusters and hydrogen in SiN_x:H films: Influence of high hydrostatic pressure under annealing. Thin Solid Films. 2012;**520**:6207-6214. DOI: 10.1016/j.tsf.2012.05.019

[25] Gritsenko VA, Xu JB, Kwok RWM, Ng YN, Wilson IH. Short range order and the nature of defects and traps in amorphous silicon oxynitride governed by the Mott rule. Physical Review Letters. 1998;**81**:1054-1057. DOI: 10.1103/PhysRevLett.81.1054

[26] Bell FG, Ley L. Photoemission study of SiO_x ($0 \leq x \leq 2$) alloys. Physical Review B. 1988;**37**:8383-8393. DOI: 10.1103/PhysRevB.37.8383

[27] Hickmott TW, Baglin JE. Stoichiometry and atomic defects in rf-sputtered SiO_2. Journal of Applied Physics. 1979;**50**:317-323. DOI: 10.1063/1.325662

[28] Shklovskii BI, Efros AL. Electronic Properties of Doped Semiconductors. Heidelberg: Springer; 1984. p. 416

[29] Strukov DB, Snider GS, Stewart DR, Williams RS. The missing memristor found. Nature. 2008;**453**:80-83. DOI: 10.1038/nature06932

[30] Mehonic A, Shluger AL, Gao D, Valov I, Miranda E, Ielmini D, et al. Silicon oxide (SiO_x): A promising material for resistance switching? Advanced Materials. 2018;**30**:1801187. DOI: 10.1002/adma.201801187

[31] Dong LP, Jia RX, Xin B, Peng B, Zhang YM. Effects of oxygen vacancies

on the structural and optical properties of β-Ga_2O_3. Scientific Reports. 2017;**7**: 40160. DOI: 10.1038/srep40160

[32] Padovani A, Gao DZ, Shluger AL, Larcher L. A microscopic mechanism of dielectric breakdown in SiO_2 films: An insight from multi-scale modeling. Journal of Applied Physics. 2017;**121**: 155101. DOI: 10.1063/1.4979915

[33] Te JY, Gismatulin A, Volodin V, Gritsenko V, Chin A. Novel all nonmetal resistive random access memory. Scientific Reports. 2019;**9**(1):6144. DOI: 10.1038/s41598-019-42706-9